ACS NANO

www.acsnano.org

Accelerated Digital Biodetection Using Magneto-plasmonic Nanoparticle-Coupled Photonic Resonator Absorption Microscopy

Congnyu Che, Ruiyang Xue, Nantao Li, Prashant Gupta, Xiaojing Wang, Bin Zhao, Srikanth Singamaneni, Shuming Nie, and Brian T. Cunningham*

Cite This: https://doi.org/10.1021/acsnano.1c08569 Read Online

ACCESS | Metrics & More | Article Recommendations | Supporting Information

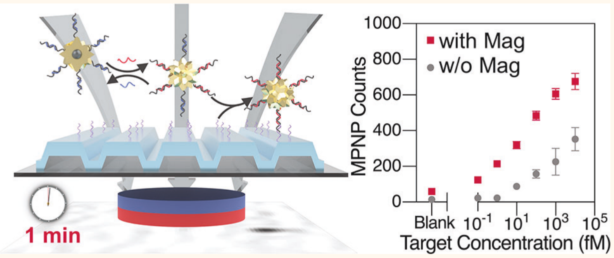

ABSTRACT: Rapid, ultrasensitive, and selective quantification of circulating microRNA (miRNA) biomarkers in body fluids is increasingly deployed in early cancer diagnosis, prognosis, and therapy monitoring. While nanoparticle tags enable detection of nucleic acid or protein biomarkers with digital resolution and subfemtomolar detection limits without enzymatic amplification, the response time of these assays is typically dominated by diffusion-limited transport of the analytes or nanotags to the biosensor surface. Here, we present a magnetic activate capture and digital counting (mAC+DC) approach that utilizes magneto-plasmonic nanoparticles (MPNPs) to accelerate single-molecule sensing, demonstrated by miRNA detection *via* toehold-mediated strand displacement. Spiky Fe_3O_4@Au MPNPs with immobilized target-specific probes are "activated" by binding with miRNA targets, followed by magnetically driven transport through the bulk fluid toward nanoparticle capture probes on a photonic crystal (PC). By spectrally matching the localized surface plasmon resonance of the MPNPs to the PC-guided resonance, each captured MPNP locally quenches the PC reflection efficiency, thus enabling captured MPNPs to be individually visualized with high contrast for counting. We demonstrate quantification of the miR-375 cancer biomarker directly from unprocessed human serum with a 1 min response time, a detection limit of 61.9 aM, a broad dynamic range (100 aM to 10 pM), and a single-base mismatch selectivity. The approach is well-suited for minimally invasive biomarker quantification, enabling potential applications in point-of-care testing with short sample-to-answer time.

KEYWORDS: *photonic crystal, magneto-plasmonic nanoparticle, fast digital detection, microRNA, strand displacement*

Liquid biopsies, whereby tumor-associated biomolecules are detected and quantified within body fluids, promise minimally invasive and personalized cancer diagnosis, therapy selection, prognosis, and management.[1−3] Among the molecular biomarkers in cancer liquid biopsy, small single-strand noncoding RNA known as microRNA (miRNA) is attracting increased attention as the medical research community develops a deeper understanding of its role in gene regulation[4−6] and their association with clinical outcomes.[7,8] For example, tumor-specific miRNA mutations or mis-expressions have been linked to tumor progression and metastasis, resulting in various cancer types and stages.[9,10] However, the distinctive characteristics of miRNA, such as their short length (~22 nucleotides), low abundance (femtomolar level or lower), and the potential presence of sequence variants, pose challenges for conventional detection approaches.[11,12] Present paradigms for miRNA detection, such as quantitative reverse transcription polymerase chain reaction (RT-qPCR), Northern blotting, and microarrays, are limited in their applications for point-of-care (POC) rapid analysis due to a combination of expensive equipment, time-consuming workflows, and low sensitivity.[13−16] Ultrasensitive, highly selective, rapid, simple, and cost-effective miRNA diagnostic approaches are increasingly demanded to address gaps in the capabilities of currently available methods.

Nanoparticle tags offer a route toward digital-resolution biomarker detection without chemical or enzymatic amplification due to the distinct physical and chemical properties that enable them to be detected individually with high signal-to-noise ratio. For instance, localized surface plasmon resonance

Received: September 29, 2021
Accepted: January 11, 2022

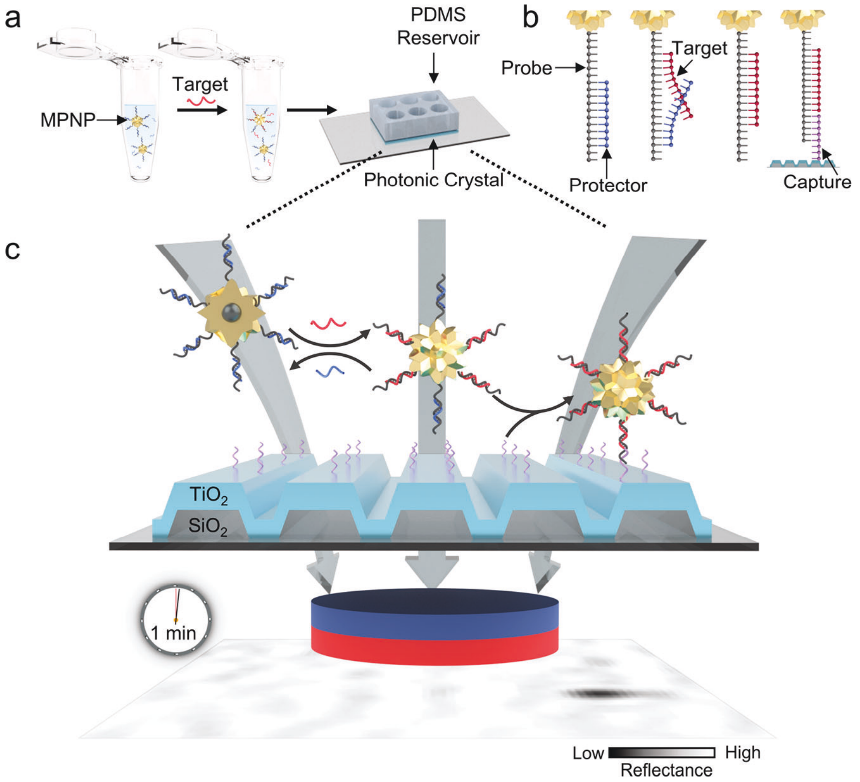

Figure 1. Schematic of miRNA quantification workflow using mAC+DC. (a) Nucleic acid toehold probe-modified MPNPs (DNA-MPNPs) are mixed with target miRNA and introduced into a PDMS reservoir attached on the PC biosensor. (b) DNA probe (gray) is preannealed with a partially complementary protector (blue) to avoid nonspecific bindings. In the presence of target miRNA (red), DNA-MPNPs are "activated" through displacement of the protector, resulting in the exposure of an additional DNA probe sequence. (c) DNA-MPNPs are simultaneously concentrated in the vicinity of the PC surface by magnetic attraction and allowed to be selectively hybridized to the capture probes (purple) immobilized on the PC surface. From the scanned PRAM image, each captured MPNP is digitally counted as the indicator of target miRNA.

(LSPR) of plasmonic nanoparticles confines light to a volume smaller than the optical diffraction limit and thus provides an absorption cross section that is much larger than their physical size and extraordinary sensitivity against superficial perturbations.[17−19] Based on this principle, surface plasmon resonance (SPR) imaging measurements[20] and interferometric reflectance imaging sensing (IRIS)[21] have achieved digital detection of nucleic acid targets with femtomolar sensitivity. However, these sensing approaches are typically based on quasi-planar transducers, and the underlying challenge is that the response time required to bind sufficient molecules or nanoparticles upon the sensing interface is limited by the slow mass transport rate.[22−24] As a result, detection of low-abundance targets can extend to hours in order to generate a signal above the background noise level. It is already common practice for bioanalytical technologies to use functionalized magnetic particles to bind with analytes in solution, followed by magnetic separation from the bulk of the test sample.[25] For example, through the use of magnetic microparticles, the single-molecule array (Simoa) technology reported detection of miRNA from human serum with high sensitivity but requires enzymatic amplification and multiple washing steps.[26] More recently, bifunctional magneto-plasmonic nanoparticles (MPNPs) have been demonstrated with combined characteristics of wavelength-tunable LSPR and paramagnetism. In previous studies, MPNPs were integrated with electrochemical biosensors[27,28] or lateral flow sensors[29] for qualitative nucleic acid and protein detection. In this work, we represent the utilization of MPNPs in digital-resolution biomolecule detection, where the plasmonic resonance of MPNP is coupled to a photonic crystal (PC) biosensor to obtain attomolar detection limits, while the magnetic properties are exploited to reduce the assay response time to 1 min.

Recently, we reported a form of biosensor microscopy called photonic resonator absorption microscopy (PRAM) that is capable of visualizing individual gold nanoparticles (AuNPs) on the surface of a PC biosensor.[30] Using PRAM as an imaging-based detection method, a digital-resolution biomolecular assay called activate capture + digital counting (AC+DC) was demonstrated for highly sensitive and selective quantification of nucleic acids and proteins.[19,31,32] In the AC+DC assay, functionalized AuNPs are activated by target molecules and selectively pulled down to a PC biosensor surface immobilized with capture probes. Utilizing the enhanced absorption of the AuNPs induced by the synergistic plasmonic−photonic coupling,[33,34] each captured AuNP on the PC surface is digitally counted with high signal-to-noise ratio, thus enabling single-particle resolution detection. While the AC+DC approach demonstrates attomolar sensitivity for nucleic acid quantification over 5 logs of dynamic range, the response time of the assay is limited by mass transport of activated AuNPs to the PC biosensor surface, which requires 2 h for 100 aM concentrations.[19]

In the present work, we aim to overcome the mass transport limit of the AC+DC assay through the use of bifunctional MPNPs. We demonstrate magnetic AC+DC (mAC+DC) in

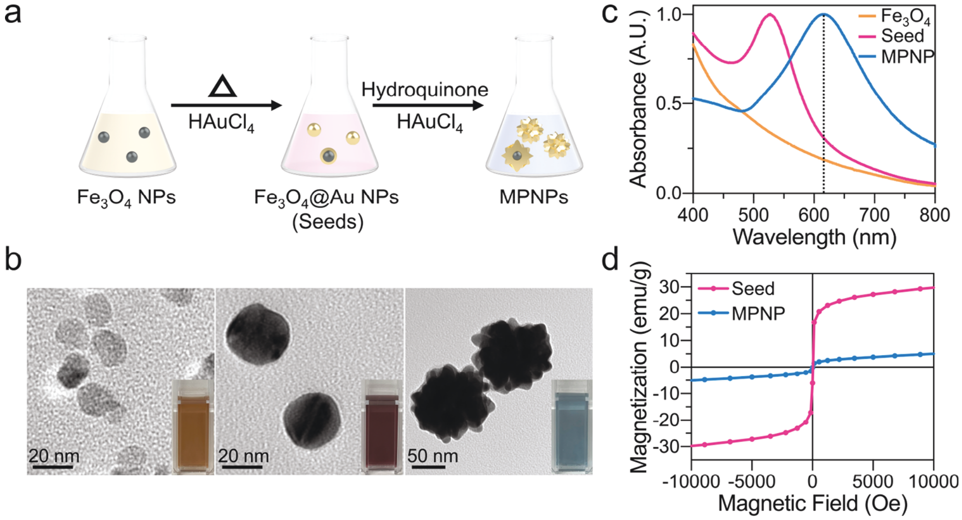

Figure 2. Characterization of MPNPs. (a) Schematic for preparation of spiky Au-coated MPNPs using a two-step self-assembly approach. The synthesis starts from coating Fe_3O_4 NPs with a smooth gold layer to produce spherical Fe_3O_4@Au core−shell seeds. Then the seeds will self-assemble with *in situ*-generated AuNPs to form the spiky MPNPs. (b) Transmission electron microscopy images of Fe_3O_4 NPs, Fe_3O_4@Au seeds, spiky MPNPs, along with photographs of corresponding aqueous dispersions in cuvettes. (c) Normalized UV−visible absorption spectra of aqueous dispersions of Fe_3O_4 NPs, Fe_3O_4@Au seeds, and spiky MPNPs. (d) Measured magnetization moments of seed and spiky MPNP solutions as a function of applied magnetic field at room temperature.

the context of detecting a specific miRNA biomarker, although the approach can be applied broadly to any other nucleic acid or protein targets. Our approach achieves three major benefits simultaneously for digital-resolution biosensing: (1) size-controlled spiky gold-coated iron oxide (Fe_3O_4@Au) MPNPs offer facile control of the LSPR wavelength to match the PC resonance wavelength, allowing for single-particle resolution imaging with high signal-to-noise ratio by PRAM; (2) the magnetic actuation of MPNPs rapidly transports analytes to the vicinity of the PC surface, yielding short response time; (3) by incorporating a thermodynamically optimized miRNA detection assay based on toehold-mediated strand displacement (TMSD), we demonstrate ultrahigh sensitivity and selectivity against single-base mismatches for a miRNA target sequence. We show that mAC+DC enables ultrasensitive (attomolar level) quantification of prostate cancer biomarker miR-375 in both buffer and unprocessed human serum, offering the potential for rapid diagnosis, prognosis, and monitoring of early stage prostate cancer in a minimally invasive fashion under POC settings.

RESULTS AND DISCUSSION

Principle of miRNA Detection by mAC+DC. The principle of the ultrafast and ultrasensitive quantification of miRNA using mAC+DC is illustrated in Figure 1. Initially, synthesized spiky MPNPs (∼90 nm in diameter) with an iron oxide core and a gold shell were functionalized with thermodynamically optimized nucleic acid toehold probes. When the hybrid probe-MPNPs were mixed with target miRNA and introduced into a poly(dimethylsiloxane) (PDMS) reservoir on the PC biosensor (Figure 1a), some MPNPs were "activated" by the target miRNA through TMSD, leading to the displacement of a protector strand. Removal of the protector exposed an additional DNA probe sequence, allowing the complement sequence immobilized on the PC biosensor to selectively capture the activated MPNP, whereas inactivated MPNPs do not have the ability to bind (Figure 1b). Meanwhile, an external magnetic field was applied with a stationary magnet placed below the PC during the incubation step to transport MPNPs through the bulk fluid and concentrate them in the vicinity of the PC sensor surface, allowing fast binding of the activated MPNPs (Figure 1c). The magnetic actuation time was optimized to foster sufficient binding events and relatively low nonspecific bindings. After the magnetic actuation, the PC surface area was imaged immediately by the PRAM instrument. The PC-captured MPNPs were resolvable at single-particle resolution with high contrast through the synergistic coupling between the LSPR of MPNPs and the PC resonance. Each captured MPNP efficiently and locally quenched the PC resonant reflection, resulting in a clearly observable dark spot in the reflected intensity. After image reconstruction and processing, a blob detection algorithm was utilized to identify the individual specifically captured MPNPs based on the size and shape of the patterns on the PRAM images to derive a count of PC-captured MPNPs, which served as the measured output of the assay.

Characterization and Visualization of MPNPs. The MPNPs were synthesized using a previously reported self-assembly process[35] with modifications to obtain paramagnetism while also matching the LSPR wavelength to the PC resonance wavelength, which is crucial in the formation of a synergistic plasmonic−photonic hybrid resonator. As shown in Figure 2a, synthesis started with citrate-stabilized spherical Fe_3O_4 NPs with a diameter of ∼20 nm (Figure 2b), which provided a relatively large magnetic saturation while avoiding becoming irreversibly magnetized. A thin layer of Au was deposited on the iron oxide cores *via* reduction of Au^{3+} using citrate as a reducing agent at high temperature, resulting in the formation of smooth spherical Fe_3O_4@Au core−shell particles with a diameter of ∼35 nm (Figure 2b). The resulting particles served as seeds for the self-assembly of the final spiky MPNPs. Rather than citrate, hydroquinone was utilized as the reducing agent to produce the spiky branches due to their more negative redox potential, enabling fast formation of *in situ*-generated AuNPs on seeds for self-assembly.[36,37] Notably, the size and morphology of the synthesized MPNPs can be easily controlled by varying the amount of seeds added, resulting in facilely tunable LSPR wavelength (Figure S1a). As shown in Figure 2c, the optimized MPNPs (average diameter ~90 nm, Figure 2b and Figure S1b) exhibit a maximum absorption wavelength of 620 nm according to the UV−visible absorption spectrum, which closely matches the 625 nm resonant wavelength of the PC. Figure 2d shows the magnetic hysteresis loop measurements of spherical Fe_3O_4@Au seeds and spiky MPNPs at room temperature using the SQUID technique. Both seeds and MPNPs clearly show superparamagnetic behavior with a saturation magnetization (M_s) of 32.6 and 6.6 emu g^{-1}, respectively. The M_s of MPNPs drops 20 times compared with that of the initial MNPs due to the diamagnetic gold coating.[35] While previous studies have reported that partial substitution of Fe^{3+} with other divalent cations (Zn^{2+}, Mn^{2+}, Co^{2+}) exhibited significantly enhanced M_s values of MPNPs,[38−41] the synthesis methods were typically complicated and time-consuming thus not used in this study.

The rugged exterior surface of spiky MPNPs facilitates effective attachment of a high density of capture molecules and a larger electromagnetic field enhancement at the tips of the spikes compared to that of a spherical particle.[42] However, spiky nanoparticles are thermodynamically unstable and can potentially transform into spherical nanoparticles or become aggregated over time.[43] Thus, a biocompatible triblock copolymer, Pluronic F-127 (poly(ethylene oxide)−poly(propylene oxide)−poly(ethylene oxide)), was utilized as a stabilizer to provide long-term colloidal stability. As a result, the MPNPs capped with F-127 displayed an increase of ~15 nm in hydrodynamic diameter (Figure S3) and maintained the branched structure for months at room temperature without morphology variation and aggregation. In the miRNA detection assay, to fabricate the DNA-MPNP conjugates, we first conjugated the heterobifunctional polyethylene glycol (SH-PEG-NHS) linker with streptavidin (SA) *via* NHS activation and reaction, as shown in Figure S4. The prepared SH-PEG-SA complex was modified onto the surface of MPNPs *via* a gold−thiol interaction. Highly specific biotinylated toehold probes for our miRNA target were conjugated onto the SA-MPNPs through the robust avidin−biotin interaction. As a gauge of conjugation performance, dynamic light scattering (DLS) measurements show an increase of ~40 nm in hydrodynamic diameter on prepared DNA-MPNPs compared to that with bare MPNPs (Figure S5). Additionally, the UV−visible spectra demonstrate that the maximum absorption wavelength shifts from 620 to 625 nm, which perfectly matches the resonance wavelength of the PC (Figure S6a). To confirm the stability of DNA-MPNPs in external magnetic field and complex media, the UV−visible spectra of DNA-MPNPs in buffer/human serum before and after being subjected to an external magnetic field for 10 min were compared. Figure S6b,c demonstrates that long magnetic actuation (10 min) in buffer/human serum (90%) results in no shift of the MPNP resonance wavelength, indicating no aggregation of the MPNPs under these situations.

To visualize single MPNPs, we utilized the PCs as resonant reflection surfaces for PRAM imaging (Figure S7). The PC is a subwavelength dielectric periodic structure designed to function as a highly efficient narrow bandwidth resonant reflector. When an incident plane wave satisfies the phase-matching condition, the PC surface will form an electromagnetic standing wave through photonic crystal-guided resonance (PCGR), resulting in a nearly 100% reflectance efficiency at the resonance wavelength.[44] We recently reported that plasmonic nanoparticles (such as MPNP) that spectrally and spatially overlap with the PCGR mode exhibit a substantially increased absorption cross section *via* synergistic electromagnetic coupling.[33,34] To examine the coupling behavior of the MPNP with the PC, through a finite-element method (FEM) simulation, we first investigated the far-field features of the PC-MPNP hybrid system. As demonstrated in Figure 3a, the LSPR wavelength of a solitary MPNP shows good agreement with the experimental data. More importantly, when coupled with a resonant PC surface, the MPNP exhibits absorption that is enhanced by approximately 4 orders of magnitude. The near-field picture of the PC-MPNP hybrid system provides insight into the origin of the observed enhancement (Figure 3b,c): the delocalized PCGR mode channels the optical energy into the dissipative MPNP, exhibiting hotspots at the tips and inside the dielectric Fe_3O_4 core. Experimentally, the enhanced optical absorption of PC-coupled MPNPs results in a localized quenching in PC reflection efficiency ($\Delta I/I \sim 10\%$, Figure S8), which is used as the contrast mechanism for image-based detection of single nanoparticles attached to a PC biosensor surface.

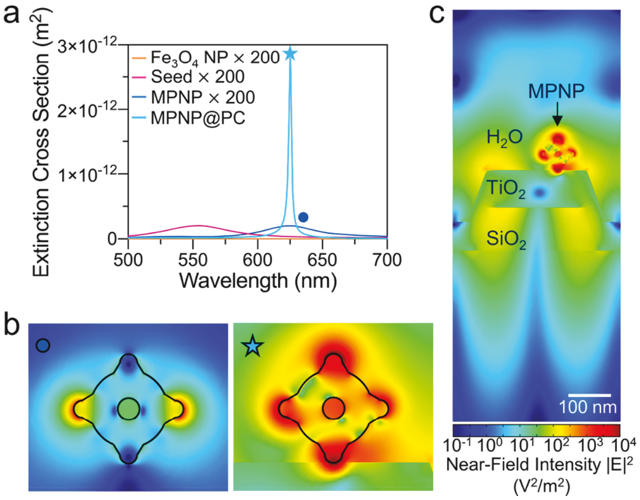

Figure 3. Numerical simulation of PC-MPNP hybrid system. (a) Extinction cross section spectra of the solitary Fe_3O_4 NP, seed, MPNP and the PC-MPNP hybrid. (b) Near-field profile of the solitary MPNP (left) and PC-MPNP hybrid (right). (c) Near-field profile of PC-MPNP hybrid under resonant condition (λ = 625 nm at normal incidence).

Optimization of the MPNP-Based mAC+DC Approach. As a proof-of-concept demonstration, we investigated miR-375 detection based on TMSD as previously reported (Figure S9).[19] We initially optimized the experimental conditions for mAC+DC system using the synthetic DNA analogue of miR-375, in which the analyte transport and capture process is manipulated and accelerated by magnetic actuation using a permanent magnet ($B \sim 0.3$ T) placed beneath the PC. The 20 nm superparamagnetic iron oxide core of the MPNP ensures large field-induced magnetic moments. To achieve higher sensitivity and speed of detection, the magnetic actuation period was optimized to offer sufficient binding events while also providing relatively low nonspecific bindings. Under the same experimental situations, three

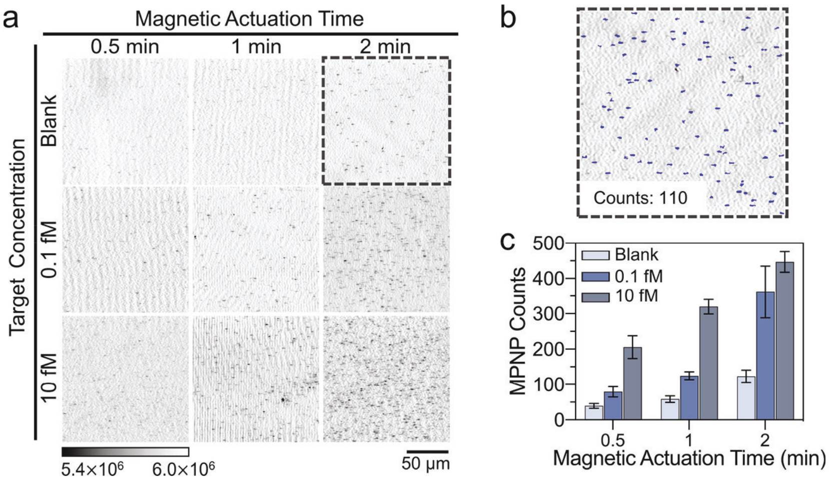

Figure 4. Optimization of the MPNP-based mAC+DC approach. (a) PRAM image panel demonstrates single-particle resolution of captured MPNPs as a function of magnetic actuation time (columns) and target concentration (rows). Blank represents the negative control performed without any target in the test sample. (b) Digital counting of bound MPNPs in the selected tile with a blob detection algorithm. The identified individual MPNPs are indicated by blue dots. (c) MPNP quantification results of the panel in (a). The error bars represent the standard deviation of three independent assays.

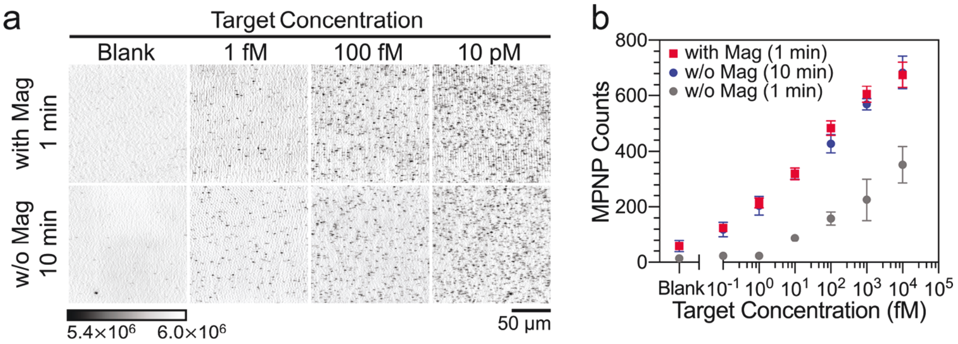

Figure 5. Quantification of the sensitivity by mAC+DC. (a) PRAM image panel demonstrates digital resolution of captured MPNPs as a function of target concentration (rows) with magnetic actuation for 1 min. A control study without magnetic actuation was performed with a 10 min incubation. (b) MPNP quantification as a function of target concentration with and without magnetic actuation. The error bars represent the standard deviation of three independent assays.

different magnetic actuation periods (0.5, 1, and 2 min) were explored to quantify three increasing concentrations of the target. The reaction mixture (total volume 10 μL) comprises 8 μL of the DNA-MPNPs (~8.9 pM), 1 μL of the target sequence, and 1 μL of $MgCl_2$ (50 mM). After the DNA-MPNPs were mixed with three defined final concentrations of target sequence (0, 0.1, and 10 fM), the resulting liquid (10 μL) was introduced into a PDMS reservoir on the PC biosensor with an external magnetic field applied for 0.5, 1, and 2 min, immediately followed by imaging using PRAM. As shown in Figure 4a, individual MPNPs captured on the PC surface can be clearly visualized, and MPNP counts, as the indicator for the presence of the target sequence, increase with the increasing target concentrations and prolonged magnetic actuation period. For the precise identification and quantification of the surface-captured single MPNPs on the 150 × 150 μm^2 scanned area, a blob detection algorithm (maximally stable extremal regions, MSER) was first applied to preliminarily segment the MPNPs from the background, followed by additional feature screening to eliminate interferers from artifacts (Figure 4b). Figure 4c demonstrates the correlation between the quantified MPNP counts with magnetic actuation period and serially decreasing target concentrations. The MPNP count is proportional to the target concentration across different magnetic actuation time periods. However, a prolonged actuation time (2 min) leads to a higher nonspecific background and a faster signal saturation, resulting in a narrower dynamic range. On the other hand, a short actuation time (0.5 min) induces ambiguity between signal from low-abundance target sequences and that of the background. An optimal actuation duration of 1 min was therefore chosen for the following miRNA detection to maintain fast response and high sensitivity.

Quantification of the Sensitivity by mAC+DC. To evaluate the analytical performance following the workflow described above, six serially diluted target sequence concentrations ranging from 100 aM to 10 pM in buffer solution (1× TE) were investigated with the previously determined optimal magnetic actuation time (1 min). A control study without magnetic actuation was conducted in parallel, with 1 and 10 min incubation times (in place of the 1 min magnetic actuation). As previously reported, without magnetic actuation, a total assay time of 2 h was required to distinguish signals of the lowest concentration (100 aM) from signals generated by no-target samples.[19] As seen in Figure 5a and Figure S10, for the 1 min magnetic actuated and 10 min diffusion-limited

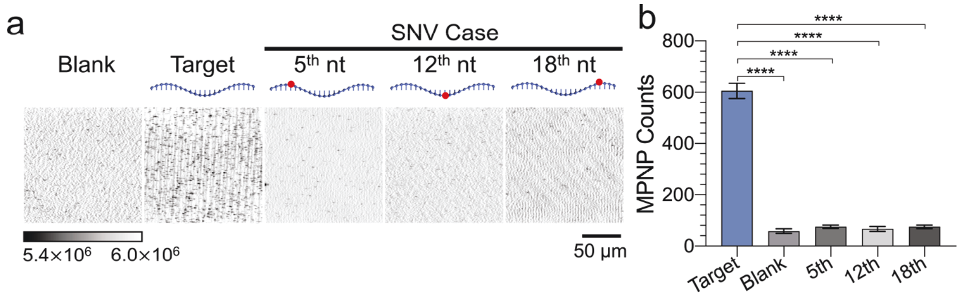

Figure 6. Single-base mismatch discrimination using mAC+DC. (a) PRAM image panel demonstrates digital resolution of captured MPNPs *versus* three different SNVs at 1 pM (columns) with 1 min magnetic actuation. (b) MPNP quantification of target sequence and the SNV cases at 1 pM concentration. Statistical significance was tested using an independent samples *t* test; ****$P < 0.0001$. The error bars represent the standard deviation of three independent assays.

cases, a higher density of MPNPs is observed with increased target concentration. In contrast, for the 1 min diffusion-limited case, the MPNP counts for lower concentrations (<1 fM) cannot be distinguished from those of the blank case with statistical significance. Figure 5b demonstrates a linear response for target sequence ranging from 100 aM to 10 pM in TE buffer. The limit of detection (LOD) is estimated from the calibration curve (Figure S11) at a MPNP count equal to the average count from a blank sample (no target) with 3 times the standard deviation. The LOD is 59.8 aM for the 1 min magnetic actuated case and 155.1 aM for the 10 min diffusion-limited case based on the linearity plot of MPNP counts *versus* log-scaled target concentration. Compared with the diffusion-limited situation, the mAC+DC approach exhibits excellent sensitivity (LOD = 59.8 aM) and a dramatically accelerated response time of 1 min, which is 10 times faster than detection without the use of magnetic forces.

Single-Base Mismatch Selectivity. To test for specificity, we investigated three different single nucleotide variants (SNVs) of the target sequence with high concentrations (1 pM) denoted by MM*x*, where *x* is the mismatch location starting from the 5′ end (Figure 6a). We compared the results of SNV cases with the no-target case and target (1 pM) case. Figure 6b indicates that the presence of a target sequence in buffer yields a maximum MPNP count, whereas the MPNP counts for SNVs and the no-target case is 5 times lower than that for the target sequence. The result demonstrates the single-base mismatch selectivity within 1 min utilizing the mAC+DC approach.

Direct Quantification of miR-375 in Human Serum. Circulating miRNAs are highly stable in human serum without degradation,[45] and the direct detection of miR-375 from serum has recently been proved to be more feasible and reliable due to the minimized variabilities between individual tests with preprocessing.[46] To demonstrate the feasibility of the mAC+DC-based digital sensing in clinical settings, miR-375 targets were spiked into crude human serum at six final target concentrations ranging from 100 aM to 10 pM, without any extraction and purification steps. Following the workflow described above with 1 min magnetic actuation time, we observed the dependency of MPNP counts on the miR-375 concentration in human serum (Figure S12a). As shown in Figure 7a, while the background signal is higher than that in TE buffer, the MPNP counts of the lowest concentration (100 aM) demonstrates higher density with statistical significance. For the human serum matrix, a similar LOD (61.9 aM) is calculated based on the linearity plot of MPNP counts *versus* log-scaled miR-375 concentration (Figure 7b and Figure S12b). We therefore conclude that the mAC+DC approach is able to quantify miR-375 directly from highly complex human serum samples with high sensitivity and a short response time of 1 min, offering the potential for rapid POC diagnostic testing of freely circulating miRNA biomarkers from a droplet-volume serum sample.

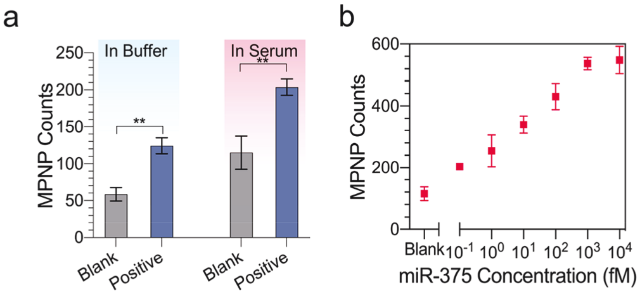

Figure 7. Direct quantification of miR-375 in human serum. (a) MPNP quantification of the no-miR-375 case and miR-375 (0.1 fM) case in buffer and human serum. Statistical significance was tested using an independent samples *t* test; **$P < 0.01$. (b) MPNP quantification in serum as a function of miR-375 concentration with 1 min magnetic actuation. The error bars represent the standard deviation of three independent assays.

CONCLUSION

In summary, we demonstrated the rapid and digital-resolution detection of miRNA biomarkers using the MPNP-based mAC+DC approach. Leveraging the resonant reflection properties of PC surfaces in conjunction with a microscopy imaging approach and highly selective nucleic acid toehold probes, the mAC+DC approach features the rapid, single-step miRNA quantification from a small volume sample with outstanding sensitivity and selectivity. The synthesis, characterization, and functionalization of the spiky gold-coated MPNPs were demonstrated, along with the high-contrast MPNP visualization by virtue of a resonance-matched PC substrate. Through FEM simulation, we investigated the synergistic PC-MPNP hybrid system upon resonance, which exhibited an enhanced absorption cross section by approximately 4 orders of magnitude, resulting in an experimentally localized quenching in PC reflection efficiency. Finally, we demonstrated the optimization and first utilization of the mAC+DC platform for prostate cancer biomarker miR-375 quantification from unprocessed human serum. A detection limit of 61.9 aM and a dynamic range that spans across 5 orders of magnitude (100 aM to 10 pM) were achieved with a response time of 1 min and single-base mismatch selectivity.

For miRNA detection under POC settings, subfemtomolar sensitivity and fast response speed are desirable, especially in body fluids where the concentration of circulating free miRNA is extremely low. However, low LOD and fast responses are typically contradictory due to the diffusion-limited mass transport of the analytes or nanoparticle tags to the sensing interface. Our approach addresses these challenges by the integration of magnetic actuation and single-molecule detection, and the attomolar-level detection limit and 1 min response time represent a capability that is not available from existing miRNA detection approaches and the gold standard PCR technique (Table S1). In our present assay, the available MPNPs far outnumber the target miRNA molecules at the lowest concentration, and our hypothesis is that target miRNA will rapidly encounter and bind with a probe on an MPNP when they are mixed together in solution. However, it may be possible to further ensure that every available miRNA will have the opportunity to encounter a toehold probe within the 1 min assay incubation time through introduction of fluid agitation or rotation of the MPNPs in a rotating magnetic field.[25] An integration of the magnetically driven rotation and transport could potentially offer both accelerated target and MPNP capture, demonstrating even lower LOD and a faster measurement. To make the mAC+DC assay more compatible with POC environments, we recently reported a cost-effective and portable PRAM instrument, whose main components are a low-power red light-emitting diode (LED) and a webcam-style CMOS image sensor,[47] thus rendering this method a promising candidate for POC diagnostics in environments such as health clinics. Due to the low volume sample size, small sensor size, and fast detection time, we also envision multiplexed assays that can be performed in adjacent fluid compartments on a single PC biosensor chip or multiple capture spots within a single well. The approach shown here is broadly applicable to the digital detection of a variety of biomarkers, such as proteins, cfDNA, and other RNAs that also have demanding requirements for low detection limits and wide dynamic range in a minimally invasive fashion.

METHODS

Materials. Fe_3O_4 NPs (20 nm, 20 mg/mL) in aqueous 2 mM sodium citrate solution were purchased from nanoComposix (San Diego, CA, USA). Sodium citrate tribasic dehydrate, gold(III) chloride trihydrate ($HAuCl_4$), hydroquinone, Pluronic F-127, streptavidin, bovine serum albumin (BSA), Tween-20, $MgCl_2$, and (3-glycidyloxypropyl)trimethoxysilane (GPTMS) were purchased from Sigma-Aldrich (St. Louis, MO, USA). SuperBlock blocking buffer in phosphate-buffered saline (PBS) was purchased from Thermo Fisher Scientific (Waltham, MA, USA). Heterobifunctional thiol polyethylene glycol succinimidyl glutaramide (SH-PEG-NHS, MW 5000) linkers were purchase from JenKem Technology (Plano, TX, USA). The DNA oligonucleotide probe with a biotinylated 3′ end, the PC capture probe with an amino-modified 3′ end, target miR-375, the DNA analogue of miR-375, and three SNVs were purchased from Integrated DNA Technologies (Coralville, IA, USA). The sequences of these oligonucleotides are listed in Table S2. Deionized water (DI water) was used in the aqueous solution preparation.

Synthesis of Spiky Core–Shell MPNPs. The spiky core–shell Fe_3O_4@Au was synthesized *via* a two-step growth method. First, the as-purchased 20 nm Fe_3O_4 NP solution (~3 μM, 25 μL) was incubated in a 20 mM sodium citrate solution (600 μL) for 30 min under moderate shaking. After the incubation, the Fe_3O_4 NPs were washed by centrifugation at 20000*g* once and then redispersed with 2 mL of 6 mM sodium citrate solution. Four milliliters of $HAuCl_4$ solution (0.5 mM) was brought to boiling, and 2 mL of the above Fe_3O_4 NP solution was quickly added under vigorous stirring. The mixture was allowed to react 10 min in the boiling state, during which time the color of the solution changed from brown to burgundy. DI water was added during the process to keep the solution volume consistent. The solution was then cooled under stirring for another 10 min, followed by centrifugation at 4000*g* three times. The resulting smooth spherical core−shell Fe_3O_4@Au NPs were redispersed to 3 mL of DI water and served as the seed for the next step. For the growth of spiky gold coating, a mixture solution of $HAuCl_4$ (0.25 mM, 5 mL), Fe_3O_4@Au seeds (Abs (535 nm) = 3.5, 100 μL), and sodium citrate (1 wt %, 11 μL) was first mixed under vigorous stirring, and then a hydroquinone solution (30 mM, 500 μL) was quickly injected to initialize the reaction. The growth solution was allowed to react for 30 min at room temperature under consistent stirring speed, during which time the solution gradually changed from pink to blue. The resulting spiky Fe_3O_4@Au MPNP solution was washed at 1000*g* three times and redispersed in 0.1% (w/v) Pluronic F-127 solution for long-term storage.

Conjugation of DNA Probes to MPNPs. The highly specific biotinylated toehold probes were conjugated to SA-MPNP through a robust avidin−biotin interaction. The modification of SA to the MPNP surface was carried out using heterobifunctional SH-PEG-NHS linkers. In detail, 23.5 μL of SH-PEG-NHS solution (4 μM) and 10 μL of SA (9.4 μM) at an equal molar ratio were mixed with 466.5 μL of PBS buffer at pH = 7.5. The resulting solution was incubated at room temperature for 2 h to allow the formation of the SH-PEG-SA complex. The mixture was further washed with 1× PBS buffer three times using a 30 kDa centrifuge filter to remove any byproduct. Next, the as-prepared SH-PEG-SA was mixed with 2.5 mL of synthesized MPNPs (Abs (620 nm) = 1.6, ~11.9 pM) and incubated overnight at 4 °C, resulting in the conjugation of SAs to the MPNP surface. Next, 125 μL of 1% BSA solution was added to the mixture and incubated for another 2 h to completely block the remaining exposed surface on the MPNP. The resulting SA-MNPT conjugates were washed twice (10 min centrifugation at 1000*g*) and redispersed with 2.5 mL of conjugation buffer containing 0.05× PBS buffer solution, 0.05× TE buffer solution, 0.625 mM $MgCl_2$, and 0.00125% Tween-20. The DNA toehold probe (10 nM) was first annealed to a protector (100 nM) in a molar ratio of 1:10 at 80 °C for 2 min and then cooled 0.5 °C every 30 s to 18 °C. After that, the annealed biotinylated DNA probes were incubated with SA-MPNPs in a molar ratio of 25:1 at 4 °C overnight, resulting in the conjugation of DNA probes to MPNPs. The prepared DNA-MPNPs were washed three times with 2.5 mL of conjugation buffer (10 min centrifugation at 1000*g*) and stored at 4 °C for further use.

Characterization of the MPNPs. The hydrodynamic size distribution of the nanoparticles was determined by DLS measurement on a Malvern Zetasizer ZS90 instrument (Malvern Panalytical, UK) at a fixed angle of 90°. UV−visible absorbance spectra were recorded on a GENESYS 10S UV−visible spectrophotometer (Thermo Scientific, USA). To determine the concentrations of the resulting spiky MPNPs, we measured the content of Fe and Au in the aqueous solution by inductively coupled plasma-optical emission spectrometry (Optima 8300).

PC Design. The PC structure used in our work comprised a low refractive index periodic grating structure that was coated with a higher refractive index material (TiO_2), as shown in Figure 1a. PCs were fabricated on glass wafers deposited with a 10 nm etch stop layer of Al_2O_3. The periodic grating patterns were constructed by depositing a layer of SiO_2 followed by large area ultraviolet interference lithography performed by Moxtek (Orem, UT, USA). Finally, a thin layer of TiO_2 (thickness ~100 nm) was deposited on the etched wafers. The resulting PC covers a surface area of 1 × 1 cm^2. The PC is designed to function as a narrowband optical resonator that optimally reflects at λ = 625 nm under water immersion.[30]

PRAM Imaging. A schematic diagram of the PRAM instrument is shown in Figure S7. The system is built upon the body of a bright-field microscope (Carl Zeiss Axio Observer Z1) with 20× or 40× objective lens as described previously.[30] The optical components consist of an optical fiber-coupled broadband LED (Thorlabs M617F1, 600 < λ < 650 nm) source, a polarizing beam splitter to collimate and filter the fiber output, and a cylindrical lens (f = 200 mm) to focus the polarized light onto the objective back focal plane. As a result, a line-profiled light beam which is perpendicular to the PC grating lines illuminates the PC from below at normal incidence through the microscope objective. The reflected light is then collected by the objective and directed to an imaging spectrometer (Acton Research) where the reflectance spectrum can be obtained by a charge-coupled device camera (Photometrics Cascade, 512 × 512 pixels). By scanning along the PC grating direction, a 2D PRAM image can be obtained by assigning the reflection peak intensity to each pixel within the scanned area.

Image Analysis. The raw PRAM images were first filtered in the Fourier plane to remove nonuniform background caused by line scanning. Next, MSER was used to detect the blob shapes presented in the images. Each detected region was then gauged with regard to its orientation, total size, eccentricity, and averaged signal intensity. Finally, the detected shapes satisfying the selection criteria were enumerated.

Numerical Simulation. 3D FEM simulations for the PC-MPNP hybrid structure in the near-field and far-field domain were conducted in COMSOL Multiphysics using the wave optics module. The unit cell of the simulation consists of one period (390 nm) of the PC structure, with a MPNP located directly on the surface of the PC ridge. Perfectly matched layer (PML) boundary condition was imposed in the direction perpendicular to the PC substrate, while the Floquet periodic boundary condition surrounds the unit cell in the transverse direction. The structural parameters of the PC resonator were extracted from previous publications[19,34] based on scanning electron microscopy characterization. Similarly, we obtained the geometric parameters of the MPNP from transmission electron microscopy images shown in Figure 2b. We employed constant refractive indices for the PC materials and superstrate within the simulated spectral region: $n_{\mathrm{TiO_2}}$ = 2.37, n_{glass} = 1.47, n_{water} = 1.33. Nonuniform mesh was established within the physical domain, with extra fine mesh imposed on in the peripheral of the MPNP. The excitation planar wave was launched at normal incidence with transverse magnetic polarization. For the simulation of the PC-enhanced MPNP absorption, the full-field solution computed under Floquet periodic condition was used as the background field for MPNP excitation with the periodic condition replaced by PML layers. The extinction cross section was then obtained by integrating the relative Poynting vector over the surface of the MPNP and normalized by the incident intensity.

Surface Functionalization of PCs for miRNA Detection Assay. The PC surface was cleaned by sonication in acetone, isopropyl alcohol, and Milli-Q water for 2 min each and dried under a stream of N_2 gas, followed by O_2 plasma treatment (Pico plasma system, diener electronic, power = 200 W, 10 min). In a glass jar, 100 μL of GPTMS was added for each PC and allowed for vapor deposition in an 80 °C vacuum oven for 4 h. The resulting PCs were sonicated in toluene, methanol, and Milli-Q water for 2 min and subsequently dried with N_2. A piece of PDMS containing six reservoirs (diameter = 3 mm) was attached onto the PC surface. For the miRNA detection assay, 20 μL of amino-modified PC capture probes (12.5 μM, in 1× TE, pH 9) was introduced into each reservoir and incubated overnight at room temperature. The reservoirs were washed by a gradual decrease of TE buffer concentration from 1× to 0.01× TE. The PC chips were stored at 4 °C until use. Before the assay was run, the capture probe-modified PC was incubated with SuperBlock blocking buffer for 80 min and washed by 1× TE buffer.

ASSOCIATED CONTENT

Supporting Information

The Supporting Information is available free of charge at https://pubs.acs.org/doi/10.1021/acsnano.1c08569.

> Supplementary figures and tables including the UV–visible spectra of spiky MPNPs with different sizes; elemental mapping analysis of MPNPs; hydrodynamic size distribution of bare, F-127-coated MPNPs; preparation of DNA-MPNPs; hydrodynamic size distribution of SA-MPNPs and DNA-MPNPs; UV–visible spectra of DNA-MPNP after magnetic actuation in buffer/serum; schematic diagram of the PRAM instrument; representative PC resonant reflected spectrum; gel electrophoresis analysis of the miR-375 detection assay; PRAM image panel for the assay; linear calibration curve of the assay; PRAM image panel and linear calibration curve for the miR-375 detection assay in serum; comparison with other miRNA detection approaches; sequences of oligonucleotide used in miR-375 detection (PDF)

AUTHOR INFORMATION

Corresponding Author

Brian T. Cunningham – *Department of Bioengineering, Nick Holonyak Micro and Nanotechnology Laboratory, Department of Electrical and Computer Engineering, and Carl R. Woese Institute for Genomic Biology, University of Illinois at Urbana—Champaign, Urbana, Illinois 61801, United States*; Email: bcunning@illinois.edu

Authors

Congnyu Che – *Department of Bioengineering and Nick Holonyak Micro and Nanotechnology Laboratory, University of Illinois at Urbana—Champaign, Urbana, Illinois 61801, United States*; orcid.org/0000-0002-8224-0803

Ruiyang Xue – *Department of Materials Science and Engineering, University of Illinois at Urbana—Champaign, Urbana, Illinois 61801, United States*

Nantao Li – *Nick Holonyak Micro and Nanotechnology Laboratory and Department of Electrical and Computer Engineering, University of Illinois at Urbana—Champaign, Urbana, Illinois 61801, United States*; orcid.org/0000-0003-2541-3445

Prashant Gupta – *Department of Mechanical Engineering and Materials Science, Institute of Materials Science and Engineering, Washington University in St. Louis, St Louis, Missouri 63031, United States*

Xiaojing Wang – *Nick Holonyak Micro and Nanotechnology Laboratory and Carl R. Woese Institute for Genomic Biology, University of Illinois at Urbana—Champaign, Urbana, Illinois 61801, United States*

Bin Zhao – *Nick Holonyak Micro and Nanotechnology Laboratory and Carl R. Woese Institute for Genomic Biology, University of Illinois at Urbana—Champaign, Urbana, Illinois 61801, United States*

Srikanth Singamaneni – *Department of Mechanical Engineering and Materials Science, Institute of Materials Science and Engineering, Washington University in St. Louis, St Louis, Missouri 63031, United States*; orcid.org/0000-0002-7203-2613

Shuming Nie – *Department of Bioengineering, Department of Materials Science and Engineering, Department of Electrical* *and Computer Engineering, and Department of Chemistry, University of Illinois at Urbana—Champaign, Urbana, Illinois 61801, United States*

Complete contact information is available at:
https://pubs.acs.org/10.1021/acsnano.1c08569

Notes

The authors declare no competing financial interest.

ACKNOWLEDGMENTS

This work is supported by the National Institutes of Health (NIH) R01 AI20683, R01 EB029805, and National Science Foundation (NSF) CBET 1900277. N.L. is supported by Zhejiang University ZJU-UIUC Joint Research Center (DREMES202001). B.Z. is supported by a Carl R. Woese Institute for Genomic Biology (IGB) fellowship in the Center for Genomic Diagnostics. The authors acknowledge the use of facilities and instrumentation supported by NSF through the University of Illinois Materials Research Science and Engineering Center DMR-1720633. The authors gratefully acknowledge the members of the Nanosensors Group (NSG) and staff in the Nick Holonyak Jr. Micro and Nanotechnology Laboratory for their support.

REFERENCES

(1) Siravegna, G.; Marsoni, S.; Siena, S.; Bardelli, A. Integrating Liquid Biopsies into the Management of Cancer. *Nat. Rev. Clin. Oncol.* **2017**, *14*, 531−548.

(2) Crowley, E.; Di Nicolantonio, F.; Loupakis, F.; Bardelli, A. Liquid Biopsy: Monitoring Cancer-Genetics in the Blood. *Nat. Rev. Clin. Oncol.* **2013**, *10*, 472−84.

(3) Bardelli, A.; Pantel, K. Liquid Biopsies, What We Do Not Know (yet). *Cancer Cell* **2017**, *31*, 172−179.

(4) Bartel, D. P. Micrornas: Genomics, Biogenesis, Mechanism, and Function. *Cell* **2004**, *116*, 281−297.

(5) Calin, G. A.; Croce, C. M. Microrna Signatures in Human Cancers. *Nat. Rev. Cancer* **2006**, *6*, 857−66.

(6) Lim, L. P.; Lau, N. C.; Garrett-Engele, P.; Grimson, A.; Schelter, J. M.; Castle, J.; Bartel, D. P.; Linsley, P. S.; Johnson, J. M. Microarray Analysis Shows That Some Micrornas Downregulate Large Numbers of Target Mrnas. *Nature* **2005**, *433*, 769−773.

(7) Esquela-Kerscher, A.; Slack, F. J. Oncomirs - Micrornas with a Role in Cancer. *Nat. Rev. Cancer* **2006**, *6*, 259−69.

(8) Garzon, R.; Calin, G. A.; Croce, C. M. Micrornas in Cancer. *Annu. Rev. Med.* **2009**, *60*, 167−79.

(9) Zhu, S.; Wu, H.; Wu, F.; Nie, D.; Sheng, S.; Mo, Y.-Y. Microrna-21 Targets Tumor Suppressor Genes in Invasion and Metastasis. *Cell Res.* **2008**, *18*, 350−359.

(10) Di Leva, G.; Garofalo, M.; Croce, C. M. Micrornas in Cancer. *Annu. Rev. Pathol.: Mech. Dis.* **2014**, *9*, 287−314.

(11) Dave, V. P.; Ngo, T. A.; Pernestig, A. K.; Tilevik, D.; Kant, K.; Nguyen, T.; Wolff, A.; Bang, D. D. Microrna Amplification and Detection Technologies: Opportunities and Challenges for Point of Care Diagnostics. *Lab. Invest.* **2019**, *99*, 452−469.

(12) Peng, Y.; Croce, C. M. The Role of Micrornas in Human Cancer. *Sig. Transduct. Target. Ther.* **2016**, *1*, 15004.

(13) Chen, C.; Ridzon, D. A.; Broomer, A. J.; Zhou, Z.; Lee, D. H.; Nguyen, J. T.; Barbisin, M.; Xu, N. L.; Mahuvakar, V. R.; Andersen, M. R.; Lao, K. Q.; Livak, K. J.; Guegler, K. J. Real-Time Quantification of Micrornas by Stem-Loop Rt-Pcr. *Nucleic Acids Res.* **2005**, *33*, e179.

(14) Lagos-Quintana, M.; Rauhut, R.; Lendeckel, W.; Tuschl, T. Identification of Novel Genes Coding for Small Expressed Rnas. *Science* **2001**, *294*, 853.

(15) Nelson, P. T.; Baldwin, D. A.; Scearce, L. M.; Oberholtzer, J. C.; Tobias, J. W.; Mourelatos, Z. Microarray-Based, High-Throughput Gene Expression Profiling of Micrornas. *Nat. Methods* **2004**, *1*, 155−61.

(16) Hunt, E. A.; Broyles, D.; Head, T.; Deo, S. K. Microrna Detection: Current Technology and Research Strategies. *Annu. Rev. Anal. Chem.* **2015**, *8*, 217−237.

(17) Kelly, K. L.; Coronado, E.; Zhao, L. L.; Schatz, G. C. The Optical Properties of Metal Nanoparticles: The Influence of Size, Shape, and Dielectric Environment. *J. Phys. Chem. B* **2003**, *107*, 668−677.

(18) Zhou, X.; Cao, P.; Zhu, Y.; Lu, W.; Gu, N.; Mao, C. Phage-Mediated Counting by the Naked Eye of Mirna Molecules at Attomolar Concentrations in a Petri Dish. *Nat. Mater.* **2015**, *14*, 1058−64.

(19) Canady, T. D.; Li, N.; Smith, L. D.; Lu, Y.; Kohli, M.; Smith, A. M.; Cunningham, B. T. Digital-Resolution Detection of Microrna with Single-Base Selectivity by Photonic Resonator Absorption Microscopy. *Proc. Natl. Acad. Sci. U. S. A.* **2019**, *116*, 19362.

(20) Aoki, H.; Corn, R. M.; Matthews, B. Microrna Detection on Microsensor Arrays by Spr Imaging Measurements with Enzymatic Signal Enhancement. *Biosens. Bioelectron.* **2019**, *142*, 111565.

(21) Sevenler, D.; Daaboul, G. G.; Ekiz Kanik, F.; Unlu, N. L.; Unlu, M. S. Digital Microarrays: Single-Molecule Readout with Interferometric Detection of Plasmonic Nanorod Labels. *ACS Nano* **2018**, *12*, 5880−5887.

(22) Kelley, S. O.; Mirkin, C. A.; Walt, D. R.; Ismagilov, R. F.; Toner, M.; Sargent, E. H. Advancing the Speed, Sensitivity and Accuracy of Biomolecular Detection Using Multi-Length-Scale Engineering. *Nat. Nanotechnol.* **2014**, *9*, 969−80.

(23) Gooding, J. J.; Gaus, K. Single-Molecule Sensors: Challenges and Opportunities for Quantitative Analysis. *Angew. Chem., Int. Ed. Engl.* **2016**, *55*, 11354−66.

(24) Squires, T. M.; Messinger, R. J.; Manalis, S. R. Making It Stick: Convection, Reaction and Diffusion in Surface-Based Biosensors. *Nat. Biotechnol.* **2008**, *26*, 417−26.

(25) van Reenen, A.; de Jong, A. M.; Prins, M. W. Accelerated Particle-Based Target Capture–the Roles of Volume Transport and near-Surface Alignment. *J. Phys. Chem. B* **2013**, *117*, 1210−8.

(26) Cohen, L.; Hartman, M. R.; Amardey-Wellington, A.; Walt, D. R. Digital Direct Detection of Micrornas Using Single Molecule Arrays. *Nucleic Acids Res.* **2017**, *45*, e137.

(27) Tavallaie, R.; McCarroll, J.; Le Grand, M.; Ariotti, N.; Schuhmann, W.; Bakker, E.; Tilley, R. D.; Hibbert, D. B.; Kavallaris, M.; Gooding, J. J. Nucleic Acid Hybridization on an Electrically Reconfigurable Network of Gold-Coated Magnetic Nanoparticles Enables Microrna Detection in Blood. *Nat. Nanotechnol.* **2018**, *13*, 1066−1071.

(28) Chen, D.; Wu, Y.; Hoque, S.; Tilley, R. D.; Gooding, J. J. Rapid and Ultrasensitive Electrochemical Detection of Circulating Tumor DNA by Hybridization on the Network of Gold-Coated Magnetic Nanoparticles. *Chem. Sci.* **2021**, *12*, 5196−5201.

(29) Ren, W.; Mohammed, S. I.; Wereley, S.; Irudayaraj, J. Magnetic Focus Lateral Flow Sensor for Detection of Cervical Cancer Biomarkers. *Anal. Chem.* **2019**, *91*, 2876−2884.

(30) Zhuo, Y.; Hu, H.; Chen, W.; Lu, M.; Tian, L.; Yu, H.; Long, K. D.; Chow, E.; King, W. P.; Singamaneni, S.; Cunningham, B. T. Single Nanoparticle Detection Using Photonic Crystal Enhanced Microscopy. *Analyst* **2014**, *139*, 1007−15.

(31) Che, C.; Li, N.; Long, K. D.; Aguirre, M. A.; Canady, T. D.; Huang, Q.; Demirci, U.; Cunningham, B. T. Activate Capture and Digital Counting (Ac + Dc) Assay for Protein Biomarker Detection Integrated with a Self-Powered Microfluidic Cartridge. *Lab Chip* **2019**, *19*, 3943−3953.

(32) Zhao, B.; Che, C.; Wang, W.; Li, N.; Cunningham, B. T. Single-Step, Wash-Free Digital Immunoassay for Rapid Quantitative Analysis of Serological Antibody against Sars-Cov-2 by Photonic Resonator Absorption Microscopy. *Talanta* **2021**, *225*, 122004.

(33) Liu, J. N.; Huang, Q.; Liu, K. K.; Singamaneni, S.; Cunningham, B. T. Nanoantenna-Microcavity Hybrids with Highly Cooperative Plasmonic-Photonic Coupling. *Nano Lett.* **2017**, *17*, 7569−7577.

(34) Huang, Q.; Cunningham, B. T. Microcavity-Mediated Spectrally Tunable Amplification of Absorption in Plasmonic Nanoantennas. *Nano Lett.* **2019**, *19*, 5297.

(35) Zhou, H.; Kim, J.-P.; Bahng, J. H.; Kotov, N. A.; Lee, J. Self-Assembly Mechanism of Spiky Magnetoplasmonic Supraparticles. *Adv. Funct. Mater.* **2014**, *24*, 1439−1448.

(36) Perrault, S. D.; Chan, W. C. W. Synthesis and Surface Modification of Highly Monodispersed, Spherical Gold Nanoparticles of 50−200 Nm. *J. Am. Chem. Soc.* **2009**, *131*, 17042−17043.

(37) Gentry, S. T.; Fredericks, S. J.; Krchnavek, R. Controlled Particle Growth of Silver Sols through the Use of Hydroquinone as a Selective Reducing Agent. *Langmuir* **2009**, *25*, 2613−2621.

(38) Seo, D.; Southard, K. M.; Kim, J. W.; Lee, H. J.; Farlow, J.; Lee, J. U.; Litt, D. B.; Haas, T.; Alivisatos, A. P.; Cheon, J.; Gartner, Z. J.; Jun, Y. W. A Mechanogenetic Toolkit for Interrogating Cell Signaling in Space and Time. *Cell* **2016**, *165*, 1507−1518.

(39) Kim, J. W.; Seo, D.; Lee, J. U.; Southard, K. M.; Lim, Y.; Kim, D.; Gartner, Z. J.; Jun, Y. W.; Cheon, J. Single-Cell Mechanogenetics Using Monovalent Magnetoplasmonic Nanoparticles. *Nat. Protoc.* **2017**, *12*, 1871−1889.

(40) Fantechi, E.; Innocenti, C.; Bertoni, G.; Sangregorio, C.; Pineider, F. Modulation of the Magnetic Properties of Gold-Spinel Ferrite Heterostructured Nanocrystals. *Nano Res.* **2020**, *13*, 785−794.

(41) Guo, J. L.; Chiou, Y. D.; Liang, W. I.; Liu, H. J.; Chen, Y. J.; Kuo, W. C.; Tsai, C. Y.; Tsai, K. A.; Kuo, H. H.; Hsieh, W. F.; Juang, J. Y.; Hsu, Y. J.; Lin, H. J.; Chen, C. T.; Liao, X. P.; Shi, B.; Chu, Y. H. Complex Oxide-Noble Metal Conjugated Nanoparticles. *Adv. Mater.* **2013**, *25*, 2040−4.

(42) Chen, H.; Kou, X.; Yang, Z.; Ni, W.; Wang, J. Shape- and Size-Dependent Refractive Index Sensitivity of Gold Nanoparticles. *Langmuir* **2008**, *24*, 5233−5237.

(43) Kotov, N. A. Inorganic Nanoparticles as Protein Mimics. *Science* **2010**, *330*, 188.

(44) Cunningham, B. T.; Li, P.; Schulz, S.; Lin, B.; Baird, C.; Gerstenmaier, J.; Genick, C.; Wang, F.; Fine, E.; Laing, L. Label-Free Assays on the Bind System. *J. Biomol. Screening* **2004**, *9*, 481−90.

(45) Chen, X.; Ba, Y.; Ma, L.; Cai, X.; Yin, Y.; Wang, K.; Guo, J.; Zhang, Y.; Chen, J.; Guo, X.; Li, Q.; Li, X.; Wang, W.; Zhang, Y.; Wang, J.; Jiang, X.; Xiang, Y.; Xu, C.; Zheng, P.; Zhang, J.; et al. Characterization of Micrornas in Serum: A Novel Class of Biomarkers for Diagnosis of Cancer and Other Diseases. *Cell Res.* **2008**, *18*, 997−1006.

(46) Cai, S.; Pataillot-Meakin, T.; Shibakawa, A.; Ren, R.; Bevan, C. L.; Ladame, S.; Ivanov, A. P.; Edel, J. B. Single-Molecule Amplification-Free Multiplexed Detection of Circulating Microrna Cancer Biomarkers from Serum. *Nat. Commun.* **2021**, *12*, 3515.

(47) Ghosh, S.; Li, N.; Xiong, Y.; Ju, Y.-G.; Rathslag, M. P.; Onal, E. G.; Falkiewicz, E.; Kohli, M.; Cunningham, B. T. A Compact Photonic Resonator Absorption Microscope for Point of Care Digital Resolution Nucleic Acid Molecular Diagnostics. *Biomed. Opt. Express* **2021**, *12*, 4637−4650.